LETTER

Lead-Free Flexible Perovskite Solar Cells with Interfacial Native Oxide Have >10% Efficiency and Simultaneously Enhanced Stability and Reliability

Min Chen,*,|| Qingshun Dong,|| Chuanxiao Xiao,|| Xiaopeng Zheng, Zhenghong Dai, Yantao Shi, Joseph M. Luther, and Nitin P. Padture*

Read Online

ACCESS | Metrics & More | Article Recommendations | SI Supporting Information

ABSTRACT: Here we demonstrate an innovative compositional and interfacial engineering approach to achieve Pb-free flexible perovskite solar cells (f-PSCs) with an unprecedented combination of the highest efficiency reported to date (10.43%), together with enhanced operational stability and mechanical reliability. The key to this approach is alloying of an $FASnI_3$ metal halide perovskite (MHP) thin film with Ge^{2+} to stabilize the Sn^{2+} oxidation state in the MHP, together with the use of a NiO_x hole-transport layer. We show that this results in the *in situ* formation of a thin amorphous GeO_2 native oxide layer at the $NiO_x/FASn_{0.9}Ge_{0.1}I_3$ interface. This layer not only passivates that critical interface but also enhances the interfacial mechanical bonding.
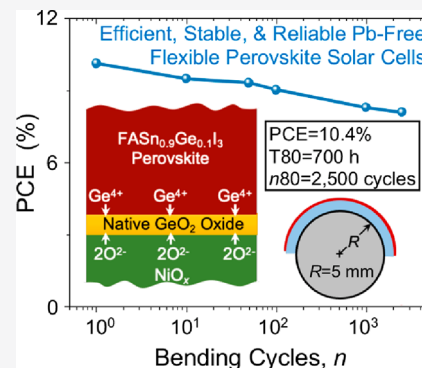
Since the first report by Miyasaka and co-workers in 2009,[1] there has been extensive research into the use of metal halide perovskites (MHPs) as light absorbers in potentially low cost solar cells.[2] As a result, the record certified power conversion efficiency (PCE) of perovskite solar cells (PSCs) now stands at 25.7%,[3] rivaling that of traditional silicon-based solar cells. PSCs have a unique advantage over other established commercial photovoltaic (PV) technologies in that they can be deposited on thin plastic substrates, which makes them highly flexible and lightweight.[4−7] Unfortunately, the MHPs used in state of the art rigid and flexible PSCs (f-PSCs) contain toxic lead (Pb), which could present a hurdle in the path toward their commercialization.[8,9] While the risk of possible Pb contamination in the case of tightly controlled utility-scale solar farms can be managed effectively, that approach may not feasible in the case of f-PSCs that are expected to be used in consumer applications such as portable chargers, wearables, tents, backpacks, deployable rollups, cars, drones, sails, etc.[4−7] Since many countries impose severe restrictions on the Pb content in consumer devices, f-PSCs could attract greater market adoption if Pb-free alternatives could be developed.[9]

A significant amount of research effort has been devoted to replacing Pb in PSCs with other lower-toxicity elements,[10]

including silver (Ag),[11] bismuth (Bi),[12] antimony (Sb),[13] titanium (Ti),[14,15] germanium (Ge),[16] tin (Sn),[17,18] and mixed Sn-Ge.[19] Among these candidates, Sn-based MHPs have shown the greatest promise[18] with the highest reported PCE of 14.7% in rigid PSCs,[20] in an attempt to close the gap between Sn-based and Pb-based PSCs. However, in the case of a Pb-free f-PSC, the highest reported PCE is quite a bit lower (8.46%).[21] The lower PCE in Sn-based PSCs in general is attributed primarily to the intrinsic instability of the Sn^{2+} oxidation state in the MHP.[22] The Sn vacancies generated during the $Sn^{2+} \rightarrow Sn^{4+}$ oxidation cause metallic conductivity,[23] and they also serve as nonradiative recombination centers for photocarriers,[24] resulting in open-circuit voltage (V_{OC}) losses.[25] Several strategies have been proposed for retaining the Sn^{2+} oxidation state in Sn-based PSCs, which include the use of antioxidants in the precursors[26−28] and defect passivation via the incorporation of bulky organic cations.[29,30] Previously we
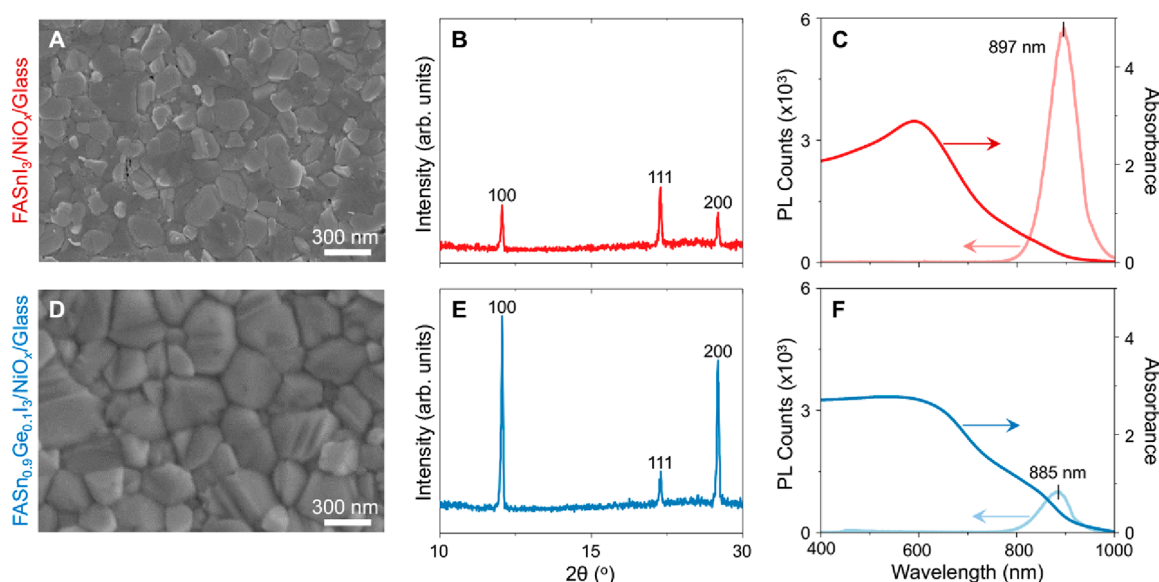
Figure 1. Characterization of the MHP thin films on NiO_x/glass substrates: top-surface SEM images of (A) $FASnI_3$ and (D) $FASn_{0.9}Ge_{0.1}I_3$; indexed XRD patterns of (B) $FASnI_3$ and (E) $FASn_{0.9}Ge_{0.1}I_3$; UV−vis absorption and PL spectra of (C) $FASnI_3$ and (F) $FASn_{0.9}Ge_{0.1}I_3$.

have shown that alloying Sn-based MHPs with Ge^{2+} as a substitutional solid solute can also result in the stabilization of Sn^{2+}, together with the formation of a stable, protective native oxide.[19] Inspired by this strategy, Nishimura et al.[31] demonstrated a PCE of over 13% in rigid PSCs incorporating GeI_2-doped Sn-based MHP thin films. It is worth noting that, unlike Pb-based PSCs, the highest PCEs in Sn-based PSCs are obtained using the p−i−n (inverted) architecture. Inverted PSCs typically utilize an organic hole-transport layer (HTL), such as poly(3,4-ethylenedioxythiophene) polystyrenesulfonate (PEDOT:PSS) or polytriarylamine (PTAA), which limits their long-term operational stability.[32] A way around this problem is to use an inorganic HTL such as nickel oxide (NiO_x). Unfortunately, the Ni^{3+} within NiO_x can react with the Sn-based MHP thin film that is in contact, resulting in Sn^{2+} → Sn^{4+} oxidation. Also, in the case of f-PSCs in general, typically they are subjected to more severe externally applied mechanical stresses during manufacturing and service (bending, stretching, twisting) in comparison to their rigid PSC counterparts, which can result in the fracture of the brittle MHP thin film, the other functional layers, and/or the interfaces.[7] Thus, enhancing the mechanical reliability of f-PSCs is particularly important.[4−7]

Here we report a new approach that addresses all of these issues in f-PSCs, and it entails Ge^{2+} alloying of Pb-free formamidinium tin triiodide ($HC(NH_2)_2SnI_3$ or $FASnI_3$) MHP thin films. We show that this results in the *in situ* growth of a thin (∼3 nm) amorphous native oxide (GeO_2) at the interface between the MHP thin film and the NiO_x HTL. The native oxide, which allows tunneling of holes while preventing the oxidation of the Sn-based MHP layer by blocking ionic diffusion, serves as a passivating layer. Also, it enhances the mechanical bonding of that critical interface. As a result, $FASn_{0.9}Ge_{0.1}I_3$-based f-PCSs show an unprecedented combination of performance metrics: the highest PCE reported so far (10.43%, with reduced hysteresis), enhanced operational stability (700 h at T_{80}, the time 80% of the initial PCE is retained) under continuous 1 sun illumination (maximum power-point (MPP) tracking, N_2 atmosphere), and enhanced mechanical reliability (2500 cycles n_{80} bending

durability, cycles (n) with 80% of the initial PCE being retained) under tension-only bending at radius $R = 5$ mm under an N_2 atmosphere.

The popular Pb-free MHP $FASnI_3$ with 5 mol % excess SnF_2, is chosen here, which has been optimized for high PCE and stability.[33] The Ge^{2+}-alloyed MHP has the composition $FASn_{0.9}Ge_{0.1}I_3$, also with 5 mol % excess SnF_2. This composition was chosen on the basis of a preliminary optimization study (not presented here). For the initial characterization experiments, thin films (∼300 nm) of these MHPs were deposited using a solvent-engineering method[34] on a NiO_x HTL on bare glass substrates, followed by annealing at 100 °C for 20 min. Figure 1A,D gives top-surface scanning electron microscope (SEM) images of the $FASnI_3$ and the $FASn_{0.9}Ge_{0.1}I_3$ thin films, respectively, showing uniform coverage. The average grain sizes are estimated to be ∼250 and ∼300 nm for the $FASnI_3$ and the $FASn_{0.9}Ge_{0.1}I_3$ thin films, respectively. The indexed X-ray diffraction (XRD) patterns of $FASnI_3$ in the $FASn_{0.9}Ge_{0.1}I_3$ thin films are presented in Figure 1B,E, respectively. While the $FASnI_3$ thin film appears to be randomly polycrystalline, the $FASn_{0.9}Ge_{0.1}I_3$ thin film shows some texture (100), which can be attributed to its relatively larger grain size.[35,36] The UV−vis spectra in Figure 1C,F of the $FASnI_3$ and the $FASn_{0.9}Ge_{0.1}I_3$ thin films respectively show comparable absorptions, but the $FASn_{0.9}Ge_{0.1}I_3$ thin film has a slightly lower Urbach energy (98 meV) in comparison to that of the $FASnI_3$ thin film (135 meV). It should be noted that the photoluminescence (PL) intensity of the $FASn_{0.9}Ge_{0.1}I_3$ thin film (Figure 1F) is significantly lower than that of the $FASnI_3$ thin film (Figure 1C), indicating much improved hole extraction at the interface with the NiO_x HTL. (The corresponding PL spectra of the MHP thin films deposited on bare glass substrates, without the NiO_x HTL, in Figure S1 in the Supporting Information show a much stronger PL signal from $FASn_{0.9}Ge_{0.1}I_3$ in comparison to $FASnI_3$, attesting to the beneficial effect of Ge^{2+} alloying.) The PL peak (∼885 nm) of the $FASn_{0.9}Ge_{0.1}I_3$ thin film is slightly blue shifted in comparison to that of the of $FASnI_3$ thin film (∼897 nm), due to the widening of the band gap by Ge^{2+} alloying.[37]
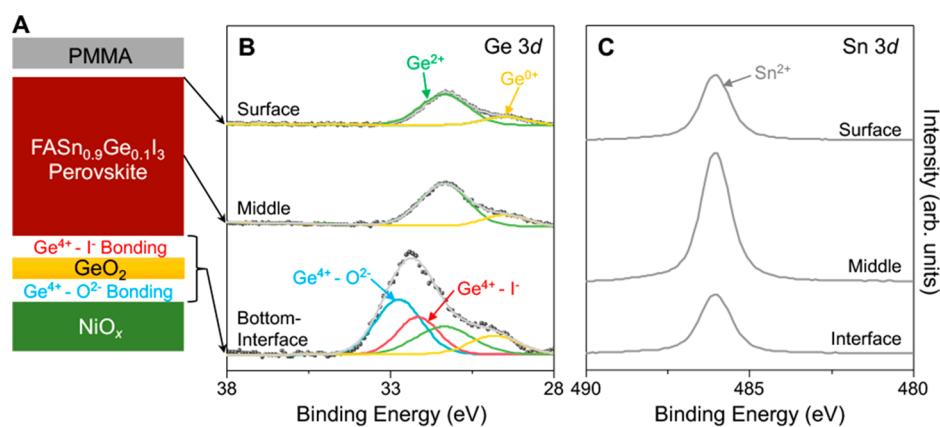
Figure 2. XPS characterization of $FASn_{0.9}Ge_{0.1}I_3$ thin films on NiO_x/glass substrates. (A) Schematic illustration (exploded view) of the depthwise XPS characterization (not to scale). Fitted and deconvoluted XPS spectra at different sputtering depths: (B) Ge 3d and (C) Sn 3d.
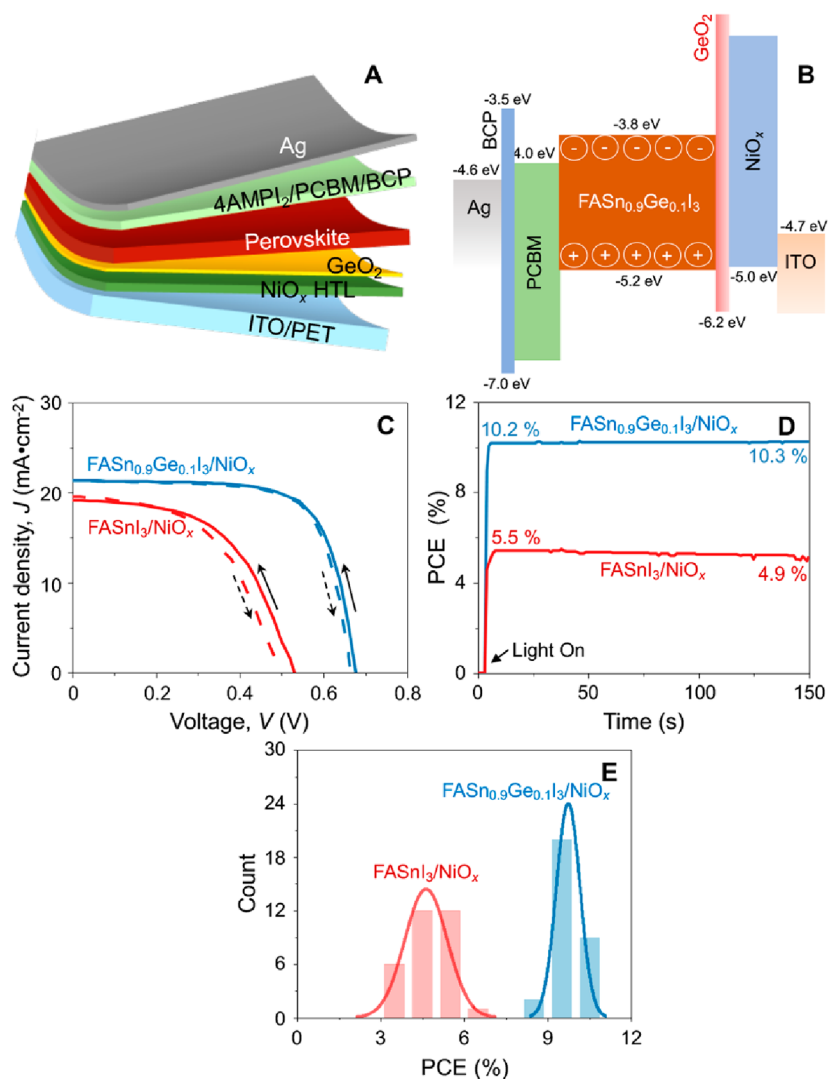

Figure 3. PV performance of $FASnI_3$-based and $FASn_{0.9}Ge_{0.1}I_3$-based f-PSCs. (A) Schematic illustration (exploded view) of the p−i−n f-PSC architecture (not to scale). (B) Corresponding energy-level diagram. (C) $J−V$ responses of "champion" f-PSC devices. (D) Stable output of "champion" f-PSC devices. (E) PCE statistics of 30 f-PSC devices each (histogram) and probability distribution (curve).

The $FASnI_3$ and the $FASn_{0.9}Ge_{0.1}I_3$ thin films on NiO_x/glass substrates were further characterized using X-ray photoelectron spectroscopy (XPS). A poly(methyl methacrylate) (PMMA) polymer layer was spin-coated on top to protect the thin film from degrading during the transfer of the samples. Here, XPS Ge 3d and Sn 3d core-level spectra were obtained at different sputtering depths. The basic scheme for depthwise XPS is illustrated in Figure 2A. The XPS Ge 3d spectra in Figure 2B
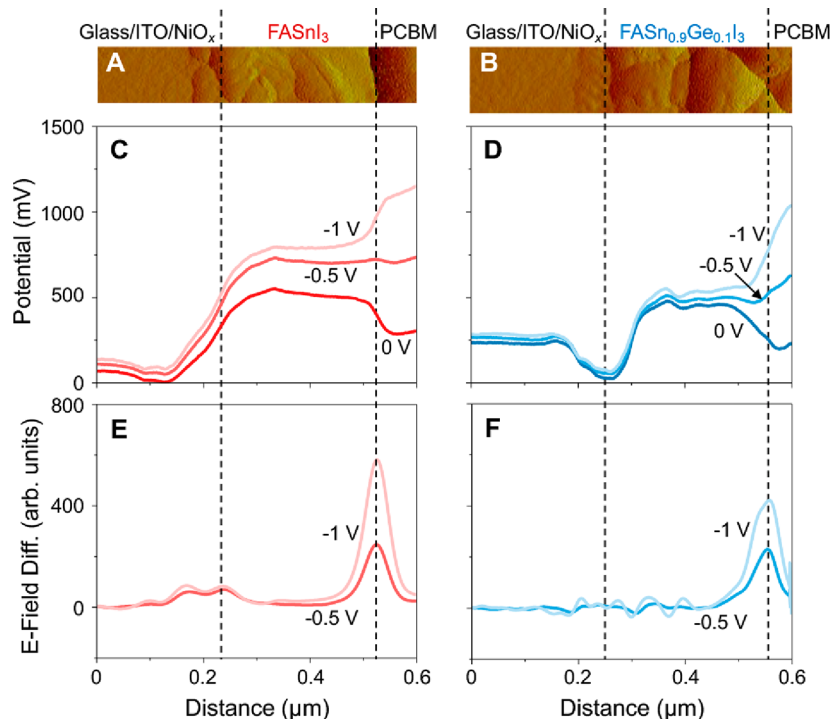
Figure 4. KPFM characterization of cross sections of rigid PSC devices. AFM images of PSCs based on (A) $FASnI_3$ and (B) $FASn_{0.9}Ge_{0.1}I_3$. Potential profiles recorded at 0, −0.5, and −1.0 V bias voltages of PSCs based on (C) $FASnI_3$ and (D) $FASn_{0.9}Ge_{0.1}I_3$. Corresponding calculated electric-field-difference profiles of PSCs based on (E) $FASnI_3$ and (F) $FASn_{0.9}Ge_{0.1}I_3$.

show that the surface and the middle part of the $FASn_{0.9}Ge_{0.1}I_3$ thin film contain mostly Ge^{2+}, with a slight amount of metallic Ge^0 being detected, which is inevitably generated due to the argon (Ar) sputtering. However, the bottom interface between the $FASn_{0.9}Ge_{0.1}I_3$ thin film and the NiO_x HTL is primarily characterized by Ge^{4+}–O^{2-} and Ge^{4+}–I^- bonding peaks. This indicates that the *in situ* grown interfacial native oxide, GeO_2, is chemically bonded with the MHP thin film (Ge^{4+}–I^-) and with the NiO_x HTL (Ge^{4+}–O^{2-}) on either side. (Note that the XPS spectra from independent standard samples, GeO_2 and GeI_4, as shown in Figure S2 in the Supporting Information, were used to identify the Ge^{4+}–O^{2-} and Ge^{4+}–I^- bonding peaks.) The XPS Sn 3d spectra in Figure 2C confirm the Sn^{2+} valence state in the entire $FASn_{0.9}Ge_{0.1}I_3$ thin film as a result of the protection provided by the interfacial GeO_2 native oxide.

Transmission electron microscopy (TEM) of the interfacial GeO_2 native oxide was also performed. Here, cross-sectional TEM specimens were carefully prepared using a focused ion beam (FIB) and were transferred to the TEM. Figure S3 in the Supporting Information is a high-angle annular dark-field (HAADF) TEM image of the cross section, and the higher resolution inset shows a thin amorphous layer (∼3 nm) sandwiched between the crystalline $FASn_{0.9}Ge_{0.1}I_3$ thin film and the NiO_x HTL. Since native oxides are typically amorphous, that layer is deemed to be the interfacial GeO_2 native oxide. Unfortunately, due to e-beam degradation in the TEM, energy dispersive spectroscopy (EDS) could not be performed reliably on that layer to characterize its chemistry. Therefore, time-of-flight secondary ion mass spectroscopy (TOF-SIMS) was performed as a function of depth. The results presented in Figure S4A in the Supporting Information clearly show the Ge-rich interfacial layer. In addition, Ge elemental maps of the top, middle, and bottom interfaces confirm the uniformly distributed abundance of Ge across the

thin film (Figure S4B−D in the Supporting Information). Further control XPS experiments were performed on both the $FASnI_3$ thin film on the NiO_x HTL and the $FASn_{0.9}Ge_{0.1}I_3$ thin film on PEDOT:PSS HTL. In the case of the former, Figure S5 in the Supporting Information shows a significant amount of Sn^{4+} at the $FASnI_3$/NiO_x interface, which is the result of a reaction with the Ni^{3+} in NiO_x. In the case of the latter, Ge^{4+} is not seen in Figure S6 in the Supporting Information, confirming the key role played by NiO_x in the *in situ* formation of the interfacial GeO_2 native oxide. Note that this native oxide formation mechanism is similar to that of GeO_2-containing native oxides in other cases, but there the oxidation source was atmospheric oxygen.[19,38]

Considering all the results from XPS, TEM, and TOF-SIMS characterization, we conclude the desirable existence of an amorphous GeO_2 native oxide of ∼3 nm thickness that has formed *in situ* at the interface between the $FASn_{0.9}Ge_{0.1}I_3$ thin film and the NiO_x HTL. The genesis of this unique GeO_2 native oxide in this system is attributed to the preferential reaction between the Ge^{2+} in the $FASn_{0.9}Ge_{0.1}I_3$ thin film and the Ni^{3+} present in the NiO_x HTL.

The $FASnI_3$ and the $FASn_{0.9}Ge_{0.1}I_3$ thin films (∼300 nm thickness) were incorporated into f-PSCs, and their PV performance, operational stability, and bending durability were evaluated. This thickness was chosen on the basis of a preliminary optimization study (not presented here). The p−i−n f-PSC architecture adopted here is illustrated in Figure 3A, and the corresponding energy-level diagram is presented in Figure 3B, where the MHP thin film is sandwiched between the NiO_x HTL and a (6,6)-phenyl-C(61)-butyric acid methyl ester (PCBM) electron-transport layer (ETL). A thin layer of an organic salt, 4-(aminomethyl) piperidinium diiodide (($(4AMP)I_2$), was spin-coated on the MHP thin film prior to PCBM deposition, which helps passivate the MHP top
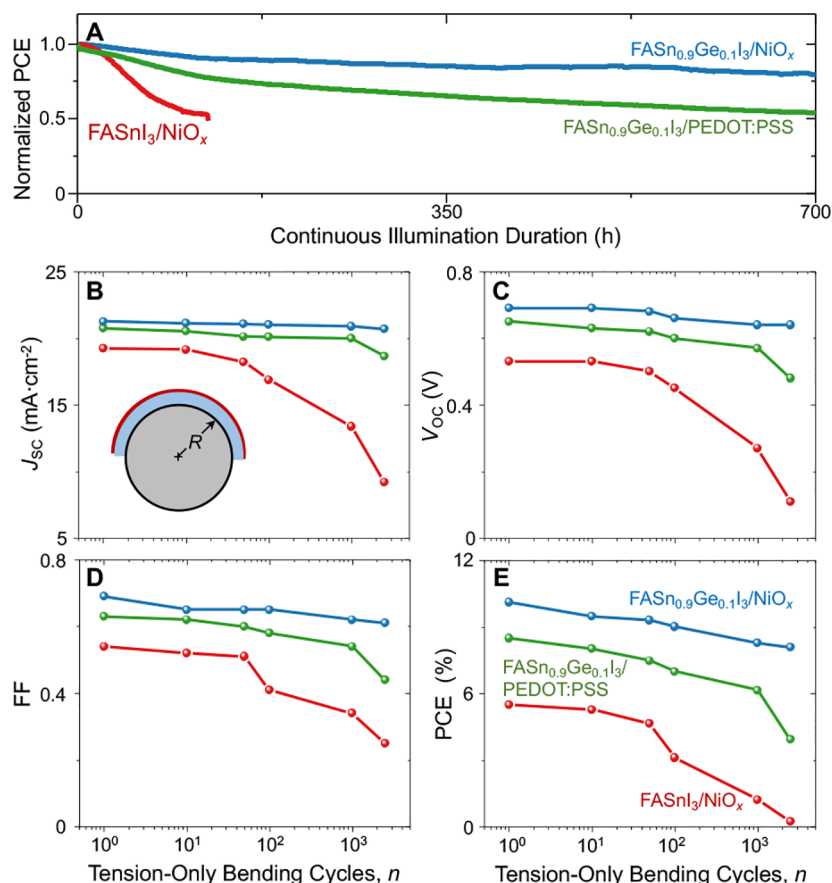
Figure 5. Operational stability and bending durability of f-PSC devices. (A) Normalized PCE of unencapsulated FASnI$_3$-based and FASn$_{0.9}$Ge$_{0.1}$I$_3$-based f-PSCs with a NiO$_x$ HTL, and FASn$_{0.9}$Ge$_{0.1}$I$_3$-based f-PSC with PEDOT:PSS HTL as a function of time under the following conditions: 1 sun continuous illumination, MPP tracking, N$_2$ atmosphere, and ~45 °C. PV parameters (B) J_{SC}, (C) V_{OC}, (D) FF, and (E) PCE of unencapsulated FASnI$_3$-based and FASn$_{0.9}$Ge$_{0.1}$I$_3$-based f-PSCs with a NiO$_x$ HTL and FASn$_{0.9}$Ge$_{0.1}$I$_3$-based f-PSC with PEDOT:PSS HTL as a function of number of bending cycles (n) under the following conditions: bending radius R = 5 mm, tension-only cycles, 1 cycle·s^{-1}, N$_2$ atmosphere, and ~25 °C. Inset in (B): schematic illustration of the bending of the PSC device around a mandrel of radius R (not to scale).

surface.[39] Additionally, a thin buffer layer of bathocuproine (BCP) was spin-coated on top of PCBM prior to the deposition of the top Ag electrode. The flexible substrate (~185 μm thickness) used here is indium tin oxide (ITO) coated polyethylene terephthalate (PET). Figure 3C plots the current density (J)−voltage (V) curves of the "champion" FASnI$_3$-based and FASn$_{0.9}$Ge$_{0.1}$I$_3$-based f-PSCs in reverse and forward scans under AM1.5G 1 sun illumination in air. The FASn$_{0.9}$Ge$_{0.1}$I$_3$-based f-PSC shows a reduced hysteresis index (H.I. = 0.043), and in a reverse scan, the V_{OC} is 0.69 V, the short-circuit current (J_{SC}) is 21.3 mA cm^{-2}, the fill factor (FF) is 0.71, and the PCE is 10.43%. This is the highest PCE ever reported for a Pb-free f-PSC. The J_{SC} value is consistent with the integrated J_{SC} calculated from the external quantum efficiency (EQE) spectrum in Figure S7 in the Supporting Information. As shown in Figure 3D, a steady PCE output of 10.3% is obtained at the MPP, which compares favorably with the extracted PCE from the J−V response, attesting to the reduced hysteresis. The evaluation of the PCE of 30 FASn$_{0.9}$Ge$_{0.1}$I$_3$-based f-PSC devices shows good reproducibility with an average PCE of 9.7 ± 0.43% (Figure 3E). The "champion" FASnI$_3$-based f-PSC device has a PCE of 5.58% in a reverse J−V scan, where the V_{OC} is 0.53 V, the J_{SC} is 19.2 mA·cm^{-2}, and the FF is 0.55. The H.I. is quite high (0.148), and the average PCE measured of 30 FASnI$_3$-based f-PSC

devices is 4.62 ± 0.83% (Figure 3E). In order to exclude the Ge^{2+} alloying effect, we also fabricated FASn$_{0.9}$Ge$_{0.1}$I$_3$-based f-PSCs, but with PEDOT:PSS HTL instead of NiO$_x$. In this case, there is no interfacial GeO$_2$ native oxide, which is confirmed in Figure S6 in the Supporting Information; the "champion" f-PSC device has a PCE of 8.50% in a reverse J−V scan, with a V_{OC} of 0.65 V, a J_{SC} of 20.8 mA·cm^{-2}, and an FF of 0.63 (Figure S8 in the Supporting Information). These PV results clearly demonstrate the beneficial effect of the interfacial GeO$_2$ native oxide in improving the PV performance of FASn$_{0.9}$Ge$_{0.1}$I$_3$-based f-PSCs with a NiO$_x$ HTL, in particular V_{OC} and FF.

To better understand the effect of the interfacial GeO$_2$ native oxide on the junction quality in these PSCs, we employed Kelvin probe force microscopy (KPFM) to characterize the cross sections of FASnI$_3$-based and FASn$_{0.9}$Ge$_{0.1}$I$_3$-based PSCs. (Note that rigid PSCs on ITO/glass substrates were used here for the convenience of obtaining clean cross sections by cleaving.) By application of small bias voltages to the devices during the measurement, KPFM spatially resolves the voltage drop across the entire device stack on a nanometer length scale.[40] The local voltage drop is determined by the equivalent resistance of different layers and interfaces,[41,42] and the junction quality can be evaluated by comparing the distribution of the voltages. Here

we took potential profiles under various bias voltages (Figures 4C,D) and deduced the corresponding electric-field differences across the device stack (Figure 4E,F) by numerically calculating the derivative of the potential changes with respect to the 0 V condition. During the scans, because the electric current through the whole device must be even, the voltage drop and the strength of the electric-field difference across the device depend on the nature of the electric junction, and they are also determined by the competition between the HTL/MHP and the MHP/ETL interfaces. In both PSCs, we observe that the main junction is located at the MHP/ETL interface (Figure 4E,F). However, in the FASnI₃-based PSC a small peak is observed at the HTL/MHP interface (Figure 4E), suggesting a leakage current across the whole device stack as a result of the poor interface between the NiO_x HTL and the FASnI₃ thin film. The NiO_x is expected to oxidize the Sn^{2+} in the FASnI₃, creating a thin metallic layer containing Sn vacancies at the interface, which can lead to the leakage current, and also enhanced recombination at that interface. However, in the case of the $FASn_{0.9}Ge_{0.1}I_3$-based PSC (Figure 4F), due to the presence of the dielectric GeO_2 native oxide at the HTL/MHP interface, no apparent leakage current is observed, and the interfacial recombination sites are expected to be reduced. These results are consistent with the higher V_{OC} and FF values observed in the $FASn_{0.9}Ge_{0.1}I_3$-based f-PSCs with a NiO_x HTL.

The operational stability of unencapsulated FASnI₃-based and $FASn_{0.9}Ge_{0.1}I_3$-based f-PSC devices with a NiO_x HTL was tested under continuous 1 sun illumination with MPP tracking (N₂ atmosphere, ∼ 45 °C). An $FASn_{0.9}Ge_{0.1}I_3$-based f-PSC with PEDOT:PSS HTL was also tested. Figure 5A shows that the PCE of the $FASn_{0.9}Ge_{0.1}I_3$-based f-PSC has degraded to 80% of its initial value after 700 h (T_{80}), whereas the PCE of the FASnI₃-based f-PSC has degraded to 50% of its initial value after 123 h. With PEDOT:PSS HTL, the PCE of the corresponding $FASn_{0.9}Ge_{0.1}I_3$-based f-PSC degraded to 53% of its initial value after 700 h. This demonstrates the clear advantage of having the GeO_2 native oxide at the NiO_x/$FASn_{0.9}Ge_{0.1}I_3$ interface to enhance the operational stability of these f-PSC devices. (Note that the paper which reports an 8.46% PCE in a Pb-free f-PSC used storage-stability tests, results from which cannot be used for comparison here.[21])

The mechanical reliability in terms of bending durability of unencapsulated FASnI₃-based and $FASn_{0.9}Ge_{0.1}I_3$-based f-PSCs with a NiO_x HTL was evaluated using an automated cyclic-bending test we have developed recently.[7] An $FASn_{0.9}Ge_{0.1}I_3$-based f-PSC with PEDOT:PSS HTL was also tested. This test entails bending of the f-PSC draped around a mandrel of radius R = 5 mm, repeatedly using a laboratory-built automated machine. Draping the entire PSC device around a mandrel ensures uniform uniaxial tensile stress in the active part of the f-PSC.[43] Here, tension-only cycles were used, where one full cycle entails a flat → convex → flat sequence, with the top surface being in uniform tension when it is convex. (Typically, one full bending cycle may entail a flat → convex → flat → concave → flat sequence, but this may result in partial crack healing during the concave (compression) part of the cycle.[43] Thus, the use of tension-only cyclic bending avoids this undesirable complication.) All experiments were conducted at 1 cycle s⁻¹ frequency, in a N₂-filled glovebox at 25 °C to preclude any environmental effects. The test was interrupted periodically, and the J−V response of the f-PSC was measured in air. The total time needed for a 2500-cycles test was ∼45 min. Figure 5B−E presents the PV parameters as a function of number of tension-only bending cycles, n. The $FASn_{0.9}Ge_{0.1}I_3$-based f-PSC with NiO_x a HTL shows a remarkable bending durability, where 80% of the initial PCE is retained after 2500 cycles (n_{80}). In comparison, the FASnI₃-based f-PSC retains only 4.5% of its initial PCE and the $FASn_{0.9}Ge_{0.1}I_3$-based f-PSC with PEDOT:PSS HTL retains 46% of its initial PCE after 2500 cycles. It is worth noting that the loss in the PCE in the last two f-PSCs is primarily the result of the rapid loss in their J_{SC} and V_{OC}. In contrast, all three PV parameters in the $FASn_{0.9}Ge_{0.1}I_3$-based f-PSC with a NiO_x HTL show gradual degradation, which is attributed to the presence of the interfacial GeO_2 native oxide in that PSC. (Note that Rao et al.[21] have conducted a different cyclic-bending test on their Pb-free f-PSCs, showing 10% reduction in the PCE after 1000 cycles.)

We have demonstrated that the use of $FASn_{0.9}Ge_{0.1}I_3$ thin films, in conjunction with a NiO_x HTL, in f-PSCs results in the *in situ* formation of a thin (∼3 nm) amorphous GeO_2 native oxide at the NiO_x/$FASn_{0.9}Ge_{0.1}I_3$ interface. This results in several desirable effects. First, the Sn^{2+} oxidation state in the MHP is better stabilized, thereby reducing the concentration of Sn vacancies and the attendant reduction in both the metallic conductivity and the concentration of recombination sites at that interface. This results in a significantly improved PCE in f-PSCs (Figure 3) over the Ge-free control f-PSCs (FASnI₃-based, with a NiO_x HTL) and the NiO_x-free control f-PSCs ($FASn_{0.9}Ge_{0.1}I_3$-based, with a PEDOT:PSS HTL). Second, the passivating interfacial GeO_2 native oxide protects the $FASn_{0.9}Ge_{0.1}I_3$ thin film, which is manifested as significantly improved operational stability over the control f-PSCs (Figure 5A). Third, the interfacial GeO_2 native oxide is expected to promote enhanced mechanical bonding between the $FASn_{0.9}Ge_{0.1}I_3$ thin film and the NiO_x HTL. This appears to be responsible for reduced delamination cracking of that critical interface under repeated bending of the f-PSCs to a relatively sharp radius (R = 5 mm), and retention of the PV function (Figure 5E).

In this context, the uniaxial applied tensile stress, $σ_A$, in the MHP thin film due to the convex bending around a cylinder of radius R can be estimated using[44]

$$σ_A = \frac{Eh}{2R} \tag{1}$$

where E is the Young's modulus of the MHP and h is the total thickness of the f-PSC. The E value of FASnI₃ has been estimated to be 8.2 GPa,[45] assuming a Poisson ratio (ν) of 0.33. (The E value of $FASn_{0.9}Ge_{0.1}I_3$ MHP has not been measured; therefore, the FASnI₃ value is used here.) Since h ≈ 185 μm, the $σ_A$ value is estimated to be ∼150 MPa. Additionally, the as-processed MHP thin film is typically under equibiaxial residual tension ($σ_R$) due to the coefficient of thermal expansion (CTE) mismatch with the substrate, which is given by[44]

$$σ_R = \frac{E(α_{MHP} - α_{ITO/PET})ΔT}{1 - ν} \tag{2}$$

where the CTE $α_{MHP}$ value for FASnI₃ is ∼37 × 10⁻⁶ °C⁻¹ [46] and that for the substrate $α_{ITO/PET}$ is ∼12 × 10⁻⁶ °C⁻¹ [47] and the temperature range through which the MHP thin film is cooled is ΔT = 77 °C (100−23 °C). (The CTE of $FASn_{0.9}Ge_{0.1}I_3$ MHP has not been measured; therefore, the

FASnI$_3$ value is used here.) Thus, σ_R is estimated to be a modest ~24 MPa, which augments the applied uniaxial tensile stress, σ_A. The combined stresses are sufficient for the MHP film to crack (channel cracking normal to the interface), considering the highly brittle nature of halide MHPs.[48] While such cracking by itself is unlikely to affect the PV performance significantly, it provides new free surfaces (edges) for the more dangerous interfacial delamination cracking to occur.[7,43,49] The driving force, or the steady-state strain-energy release rate (G), for such interfacial cracking is given by[50]

$$G = \frac{(1 - \nu^2)t\sigma_T^2}{2E} \tag{3}$$

where t (~300 nm) is the thickness of the MHP thin film, $\sigma_T = \sigma_A + \sigma_R$, and $G \geq G_C$ is the delamination cracking criterion, with G_C being the steady-state interfacial toughness. Using eq 3, the G value is estimated to be ~0.5 J·m^{-2}. While this G estimate is relatively small, it is greater than the G_C value of some of the more brittle, poorly bonded interfaces found in PSCs (as low as 0.12 J·m^{-2} [51]). The G_C values of the various interfaces in the PSCs studied here have not been measured, but it is likely that the G_C value of the NiO$_x$/FASnI$_3$ interface is similarly low. This is deemed responsible for the rapid decrease in the PCE of FASnI$_3$-based f-PSCs as the interfacial cracking damage accumulates with each bending cycle (Figure 5E). The vastly superior bending durability of FASn$_{0.9}$Ge$_{0.1}$I$_3$-based f-PSCs (Figure 5E) suggests that *in situ* formation of the GeO$_2$ native oxide effectively toughens the critical NiO$_x$/FASn$_{0.9}$Ge$_{0.1}$I$_3$ interface. It is well-known that an *in situ* grown interfacial layer between a thin film and a substrate (reaction bonding) tends to promote mechanical bonding.[50] The net result is the enhanced mechanical reliability of FASn$_{0.9}$Ge$_{0.1}$I$_3$-based f-PSCs.

In closing, f-PSCs offer some unique advantages for consumer applications, and it is desirable to remove toxic Pb from f-PSCs for better commercial prospects. Innovative approaches involving compositional and interfacial engineering, such as those presented here, to enhance all three performance metrics—efficiency, operational stability, and mechanical reliability—provide a path forward for Pb-free f-PSCs to reach their full potential.

■ ASSOCIATED CONTENT

Ⓢ Supporting Information

The Supporting Information is available free of charge at https://pubs.acs.org/doi/10.1021/acsenergylett.2c01130.

> Experimental methods, including thin-film synthesis, characterization, device fabrication, and testing, and additional references and figures (PDF)

■ AUTHOR INFORMATION

Corresponding Authors

Min Chen − School of Engineering, Brown University, Providence, Rhode Island 02912, United States; National Renewable Energy Laboratory, Golden, Colorado 80401, United States; Email: min_chen1@alumni.brown.edu

Nitin P. Padture − School of Engineering, Brown University, Providence, Rhode Island 02912, United States; orcid.org/0000-0001-6622-8559; Email: nitin_padture@brown.edu

Authors

Qingshun Dong − State Key Laboratory of Fine Chemicals, Department of Chemistry, School of Chemical Engineering, Dalian University of Technology, Dalian 116024, People's Republic of China; orcid.org/0000-0001-9498-2399

Chuanxiao Xiao − National Renewable Energy Laboratory, Golden, Colorado 80401, United States; orcid.org/0000-0002-4136-2249

Xiaopeng Zheng − National Renewable Energy Laboratory, Golden, Colorado 80401, United States; orcid.org/0000-0001-5061-3655

Zhenghong Dai − School of Engineering, Brown University, Providence, Rhode Island 02912, United States

Yantao Shi − State Key Laboratory of Fine Chemicals, Department of Chemistry, School of Chemical Engineering, Dalian University of Technology, Dalian 116024, People's Republic of China; orcid.org/0000-0002-7318-2963

Joseph M. Luther − National Renewable Energy Laboratory, Golden, Colorado 80401, United States; orcid.org/0000-0002-4054-8244

Complete contact information is available at:
https://pubs.acs.org/10.1021/acsenergylett.2c01130

Author Contributions

‖M.C., Q.D., and C.X. contributed equally.

Author Contributions

M.C. and N.P.P. conceived the idea together, designed most of the experiments, and coordinated the project. M.C. and Q.D. prepared the MHP films, fabricated the devices, and performed most of the characterization and testing experiments. C.X., X.Z., and Z.D. performed some of the characterization and testing experiments and the associated analyses. Y.S. and J.M.L. analyzed some of the results. M.C. and N.P.P. cowrote the manuscript, with input from all the other authors.

Notes

The authors declare no competing financial interest.

■ ACKNOWLEDGMENTS

■ REFERENCES

(1) Kojima, A.; Teshima, K.; Shirai, Y.; Miyasaka, T. Organometal Halid Perovskites as Visible-Light Sensitizers for Photovoltaic Cells. *J. Am. Chem. Soc.* **2009**, *131*, 6050−6051.

(2) Miyasaka, T. *Perovskite Photovoltaics and Optoelectronics: From Fundamentals to Advanced Applications*; Wiley-VCH: 2021.

(3) NREL; https://www.nrel.gov/pv/cell-efficiency.html (accessed on March 30, 2022).

(4) Jung, H. S.; Han, G. S.; Park, N.-G.; Ko, M. J. Flexible Perovskite Solar Cells. *Joule* 2019, 3, 1850−1880.

(5) Zhang, J.; Zhang, W.; Cheng, H.-M.; Silva, S. R. P. Critical review of recent progress of flexible perovskite solar cells. *Mater. Today* 2020, 39, 66−88.

(6) Tang, G.; Yan, F. Recent Progress of Flexible Perovskite Solar Cells. *Nano Today* 2021, 39, 101155.

(7) Dong, Q.; Chen, M.; Liu, Y.; Eickemeyer, F. T.; Zhao, W.; Dai, Z.; Yin, Y.; Jiang, C.; Feng, J.; Jin, S.; Liu, S.; Zakeeruddin, S. M.; Grätzel, M.; Padture, N. P.; Shi, Y. Flexible Perovskite Solar Cells with Simultaneously Improved Efficiency, Operational Stability, and Mechanical Reliability. *Joule* 2021, 5, 1587−1601.

(8) Ju, M.-G.; Chen, M.; Zhou, Y.; Dai, J.; Ma, L.; Padture, N. P.; Zeng, X. C. Towards Eco-friendly and Stable Perovskite Materials for Photovoltaics. *Joule* 2018, 2, 1231−1241.

(9) Moody, N.; Sesena, S.; deQuilettes, D. W.; Dou, B. D.; Swartwout, R.; Buchman, J. T.; Johnson, A.; Eze, U.; Brenes, R.; Johnston, M.; Haynes, C. L.; Bulovic, V.; Bawendi, M. G. Assessing the Regulatory Requirements of Lead-Based Perovskite Photovoltaics. *Joule* 2020, 4, 970−974.

(10) Ke, W.; Kanatzidis, M. G. Prospects for Low-Toxicity Lead-Free Perovskite Solar Cells. *Nature Commun.* 2019, 10, 965.

(11) Du, K.; Meng, W.; Wang, X.; Yan, Y.; Mitzi, D. B. Bandgap Engineering of Lead-Free Double Perovskite $Cs_2AgBiBr_6$ through Trivalent Metal Alloying. *Angew. Chem. Int. Ed.* 2017, 56, 8158−8162.

(12) Zhang, Z.; Li, X.; Xia, X.; Wang, Z.; Huang, Z.; Lei, B.; Gao, Y. High-Quality $(CH_3NH_3)_3Bi_2I_9$ Film-Based Solar Cells: Pushing Efficiency up to 1.64%. *J. Phys. Chem. Lett.* 2017, 8, 4300−4307.

(13) Zuo, C.; Ding, L. Lead-Free Perovskite Materials $(NH_4)_3Sb_2I_xBr_{9-x}$. *Angew. Chem. Int. Ed.* 2017, 56, 6528−6532.

(14) Chen, M.; Ju, M.-G.; Carl, A. D.; Zong, Y.; Grimm, R. L.; Gu, J.; Zeng, X. C.; Zhou, Y.; Padture, N. P. Stable Perovskite Solar Cells Based on Cesium Titanium (IV) Bromide Double Perovskite Thin Films. *Joule* 2018, 2, 558−570.

(15) Ju, M.-G.; Chen, M.; Zhou, Y.; Garces, H. F.; Dai, J.; Ma, L.; Padture, N. P.; Zeng, X. C. Earth-Abundant Non-Toxic Titanium (IV) Based Vacancy-Ordered Double Perovskite Halides with Tunable 1.0 to 1.8 eV Bandgaps for Photovoltaic Applications. *ACS Energy Lett.* 2018, 3, 297−304.

(16) Krishnamoorthy, T.; Ding, H.; Yan, C.; Leong, W. L.; Baikie, T.; Zhang, Z.; Sherburne, M.; Li, S.; Asta, M.; Mathews, N.; Mhaisalkar, S. G. Lead-Free Germanium Iodide Perovskite Materials for Photovoltaic Applications. *J. Mater. Chem. A* 2015, 3, 23829−23832.

(17) Hao, F.; Stoumpos, C. C.; Cao, D. H.; Chang, R. P. H.; Kanatzidis, M. G. Lead-Free Solid-State Organic-Inorganic Halide Perovskite Solar Cells. *Nat. Photonics* 2014, 8, 489−494.

(18) Wu, T.; Liu, X.; Luo, X.; Lin, X.; Cui, D.; Wang, Y.; Segawa, H.; Zhang, Y.; Han, L. Lead-free tin perovskite solar cells. *Joule* 2021, 5, 863−886.

(19) Chen, M.; Ju, M.-G.; Garces, H. F.; Carl, A. D.; Ono, L. K.; Hawash, Z.; Zhang, Y.; Shen, T.; Qi, Y.; Grimm, R. L.; Pacifici, D.; Zeng, X. C.; Zhou, Y.; Padture, N. P. Highly Stable and Efficient All-Inorganic Lead-Free Perovskite Solar Cells with Native-Oxide Passivation. *Nature Commun.* 2019, 10, 16.

(20) Zhou, J.; Hao, M.; Zhang, Y.; Ma, X.; Dong, J.; Lu, F.; Wang, J.; Wang, N.; Zhou, Y. Chemo-Thermal Surface Dedoping for High Performance Tin Perovskite Solar Cells. *Matter* 2022, 5, 683−693.

(21) Rao, L.; Meng, X.; Xiao, S.; Xing, Z.; Fu, Q.; Wang, H.; Gong, C.; Hu, T.; Hu, X.; Guo, R.; Chen, Y. Wearable Tin-Based Perovskite Solar Cells Achieved by a Crystallographic Size Effect. *Angew. Chem. Int. Ed.* 2021, 60, 14693−14700.

(22) Li, W.; Li, J.; Li, J.; Fan, J.; Mai, Y.; Wang, L. Addictive-Assisted Construction of All-Inorganic $CsSnIBr_2$ Mesoscopic Perovskite Solar Cells with Superior Thermal Stability up to 473 K. *J. Mater. Chem. A* 2016, 4, 17104−17110.

(23) Mitzi, D. B.; Wang, S.; Field, C. A.; Chess, C. A.; Guloy, A. M. Conducting Layered Organic-inorganic Halides Containing < 110>-Oriented Perovskite Sheets. *Science* 1995, 267, 1473−1476.

(24) Li, B.; Chang, B.; Pan, L.; Li, Z.; Fu, L.; He, Z.; Yin, L. Tin-Based Defects and Passivation Strategies in Tin-Related Perovskite Solar Cells. *ACS Energy Lett.* 2020, 5, 3752−3772.

(25) Noel, N. K.; Stranks, S. D.; Abate, A.; Wehrenfenning, C.; Guarnera, S.; Haghighirad, A.; Sadhanal, A.; Eperon, G. E.; Pathak, S. K.; Johnston, M. B.; Petrozza, A.; Herz, L. M.; Snaith, H. J. Lead-Free Organic-Inorganic Tin Halide Perovskites for Photovoltaic Applications. *Energy Environ. Sci.* 2014, 7, 3061−3068.

(26) Chung, I.; Lee, B.; He, J.; Chang, R. P. H.; Kanatzidis, M. All-Solid-State Dye-Sensitized Solar Cells with High Efficiency. *Nature* 2012, 485, 486−490.

(27) Song, T.-B.; Yokoyama, T.; Aramaki, S.; Kanatzidis, M. G. Performance Enhancement of Lead-Free Tin-Based Perovskite Solar Cells with Reducing Atmosphere-Assisted Dispersible Additive. *ACS Energy Lett.* 2017, 2, 897−903.

(28) Jiang, X.; Li, H.; Zhou, Q.; Wei, Q.; Wei, M.; Jiang, L.; Wang, Z.; Peng, Z.; Wang, F.; Zang, Z.; Xu, K.; Hou, Y.; Teale, S.; Zhou, W.; Si, R.; Gao, X.; Sargent, E. H.; Ning, Z. One-Step Synthesis of SnI_2·$(DMSO)_x$ Adducts for High-Performance Tin Perovskite Solar Cells. *J. Am. Chem. Soc.* 2021, 143, 10970−10976.

(29) Wang, F.; Jiang, X.; Chen, H.; Shang, Y.; Liu, H.; Wei, J.; Zhou, W.; He, H.; Liu, W.; Ning, Z. 2D-Quasi-2D-3D Hierarchy Structure for Tin Perovskite Solar Cells with Enhanced Efficiency and Stability. *Joule* 2018, 2, 2732−2743.

(30) Shao, S.; Nijenhuis, M.; Dong, J.; Kahmann, S.; Brink, G. H. t.; Portale, G.; Loi, M. A. Influence of the stoichiometry of tin-based 2D/3D perovskite active layers on solar cell performance. *J. Mater. Chem. A* 2021, 9, 10095−10103.

(31) Nishimura, K.; Kamarudin, M. A.; Hirotani, D.; Shen, Q.; Minemoto, T.; Yoshino, K.; Hayase, S. Pb-Free Sn-Perovskite Solar Cells with Over 13% Efficiency. *Proc. SPIE, Organic, Hybrid, and Perovskite Photovoltaics XXI* 2020, 114740X.

(32) Manders, J. R.; Tsang, S.-W.; Hartel, M. J.; Lai, T.-H.; Chen, S.; Amb, C. M.; Reynolds, J. R.; So, F. Solution-Processed Nickel Oxide Hole Transport Layers in High Efficiency Polymer Photovoltaic Cells. *Advanced Funct. Mater.* 2013, 23, 2993−3001.

(33) Meng, X.; Wang, Y.; Lin, J.; Liu, X.; He, X.; Barbaud, J.; Wu, T.; Noda, T.; Yang, X.; Han, L. Surface-Controlled Oriented Growth of $FASnI_3$ Crystals for Efficient Lead-free Perovskite Solar Cells. *Joule* 2020, 4, 902−912.

(34) Jeon, N. J.; Noh, J. H.; Kim, Y. C.; Yang, W. S.; Ryu, S.; Seok, S. I. Solvent Engineering for High-Performance Inorganic-Organic Hybrid Perovskite Solar Cells. *Nat. Mater.* 2014, 13, 897−903.

(35) Zhou, Y.; Game, O. S.; Pang, S.; Padture, N. P. Microstructures of Organometal Trihalide Perovskites for Solar Cells: Their Evolution from Solutions and Characterization. *J. Phys. Chem. Lett.* 2015, 6, 4827−4839.

(36) Dunlap-Shohl, W. A.; Zhou, Y.; Padture, N. P.; Mitzi, D. B. Synthetic Approaches for Halide Perovskite Thin Films. *Chem. Rev.* 2019, 119 (5), 3193−3295.

(37) Ito, N.; Kamarudin, M. A.; Hirotani, D.; Zhang, Y.; Shen, Q.; Ogomi, Y.; Iikubo, S.; Minemoto, T.; Yoshino, K.; Hayase, S. Mixed Sn−Ge Perovskite for Enhanced Perovskite Solar Cell Performance in Air. *J. Phys. Chem. Lett.* 2018, 9, 1682−1688.

(38) Wu, Y.-H; Wu, M.-L.; Lyu, R.-J.; Wu, J.-R.; Lin, C.-C.; Chen, L.-L. Comparison of Ge Surface Passivation Between $SnGe_x$ Films Formed by Oxidation of Sn/Ge and Sn/Ge_x/Ge Structures. *IEEE Electron Device Lett.* 2011, 32, 611−613.

(39) Hu, M.; Chen, M.; Guo, P.; Zhou, H.; Deng, J.; Yao, Y.; Jiang, Y.; Gong, J.; Dai, Z.; Zhou, Y.; Qian, F.; Chong, X.; Feng, J.; Schaller, R. D.; Zhu, K.; Padture, N. P.; Zhou, Y. Sub-1.4 eV Bandgap Inorganic Perovskite Solar Cells with Long-Term Stability. *Nature Commun.* 2020, 11, 151.

(40) Cui, P.; Wei, D.; Ji, J.; Huang, H.; Jia, E.; Dou, S.; Wang, T.; Wang, W.; Li, M. Planar $p−n$ Homojunction Perovskite Solar Cells with Efficiency Exceeding 21.3%. *Nature Energy* 2019, 4, 150−159.

(41) Xiao, C.; Wang, C.; Ke, W.; Gorman, B. P.; Ye, J.; Jiang, C.-S.; Yan, Y.; Al-Jassim, M. M. Junction Quality of SnO_2-Based Perovskite Solar Cells Investigated by Nanometer-Scale Electrical Potential Profiling. *ACS Appl. Mater. Interface* **2017**, *9*, 38373−38380.

(42) Xiao, C.; Zhang, F.; Chen, X.; Yang, M.; Harvey, S. P.; Beard, M. C.; Berry, J. J.; Jiang, C.-S.; Al-Jassim, M. M.; Zhu, K. SMART Perovskite Growth: Enabling a Larger Range of Process Conditions. *ACS Energy Lett.* **2021**, *6* (2), 650−658.

(43) Yadavalli, S. K.; Dai, Z.; Zhou, H.; Zhou, Y.; Padture, N. P. Facile Crack-Healing in Organic-Inorganic Halide Perovskite Thin Films. *Acta Mater.* **2020**, *187*, 112−121.

(44) Rolston, N.; Bush, K. A.; Printz, A. D.; Gold-Parker, A.; Ding, Y.; Toney, M. F.; McGehee, M. D.; Dauskardt, R. H. Engineering Stress in Perovskite Solar Cells to Improve Stability. *Adv. Energy Mater.* **2018**, *8*, 1802139.

(45) Lee, Y.; Mitzi, D. B.; Barnes, P. W.; Vogt, T. Pressure-Induced Phase Transitions and Templating Effect in Three-Dimensional Organic-Inorganic Hybrid Perovskites. *Phys. Rev. B* **2003**, *68*, 020103.

(46) Dang, Y.; Zhou, Y.; Liu, X.; Ju, D.; Xia, S.; Xia, H.; Tao, X. Formation of Hybrid Perovskite Tin Iodide Single Crystals by Top-Seeded Solution Growth. *Angew. Chem. Int. Ed.* **2016**, *55*, 3447−3450.

(47) Chien, C.-H.; Chen, T.; Su, F.-I.; Lin, C.-Y.; Su, T.-H.; Lin, Y.-M.; Liu, Y.-C.; Tsay, T.-L. Thickness Effects on the Thermal Expansion Coefficient of Indium Tin Oxide/Polyethylene Terephthalate Film. *Expt.Technol.* **2016**, *40* (2), 639−644.

(48) Ramirez, C.; Yadavalli, S. K.; Garces, H. F.; Zhou, Y.; Padture, N. P. Thermo-Mechanical Behavior of Organic-Inorganic Halide Perovskites for Solar Cells. *Scripta Mater.* **2018**, *150*, 36−41.

(49) Dai, Z.; Yadavalli, S. K.; Chen, M.; Abbaspourtamijani, A.; Qi, Y.; Padture, N. P. Interfacial Toughening with Self-Assembled Monolayers Enhances Perovskite Solar Cells Reliability. *Science* **2021**, *372*, 618−622.

(50) Freund, L. B.; Suresh, S. *Thin Film Materials: Stress, Defect Formation and Surface Evolution*; Cambridge University Press: 2003.

(51) Rolston, N.; Watson, B. L.; Bailie, C. D.; McGehee, M. D.; Bastos, J. P.; Gehlhaar, R.; Kim, J.-E.; Vak, D.; Mallajosyula, A. T.; Gupta, G.; Mohite, A. D.; Dauskardt, R. H. Mechanical Integrity of Solution-Processed Perovskite Solar Cells. *Ext. Mech. Lett.* **2016**, *9*, 353−358.